Research Gate

- **Abstract:**
- **Methodology:**
- **Conversion of Sunlight into Electricity**
- **Results**
- **Thin film fabrication and device performance**

❖ **Abstract:**

With a population of 1.4 billion and one of the world's fastest-growing major economies, India will be vital for the future of the global energy markets. The Government of India has made its impressive progress in recent years in attaining self-sufficiency in producing green energy through National Solar Energy Mission-2020. Report on India 2020 energy policy review states that India successfully implemented a range of energy market reforms and carried out a huge amount of renewable electricity deployment, notably in solar energy and other renewable including wind energy. It is recognised that India is one among the several countries of the world and has made huge strides to ensure full access to electricity, bringing power to more than 700 million people since 2000. By the end of 2030 India is planned to bring secure, affordable and sustainable energy to all its citizens so that India can make its significant progress in reducing the use of traditional biomass in cooking. The chief cause of indoor air pollution that particularly affects women and children is mainly due to the use of traditional use of firewood and other carbon emission fuels by relying more on green energy for cooking and other Domestic requirements including irrigation.

Methodology:

In this study, the electricity generated from the rooftop grid-tied solar power system can be calculated by the PVSYST software. The yield factor and performance ratio in PVSYST program are determined as below:
PV array yield (Ya):

$$Y_a = \frac{E_a}{P_0}$$

(1)where: P0 is the power of PV array [kWp]; Ea is output PV array yield [kWh]; Ya (Array Yield) is the PV array daily output energy, referred to the nominal power [kWh/kWp/day].
Reference system yield (Yr) is calculated by the equation:

$$Y_r = \frac{H_t}{G_0}$$

(2)where: Yr (Reference system yield) is numerically equal to the incident energy in the PV array plane [kWh/m2/day]. Ht is the total horizontal irradiance on PV array [kWh/m2] and Go is the global irradiance at standard condition (STC) (W/m2).
The system yield (Yf) equation is as below:

$$Y_f = \frac{E_{ACout}}{P_{max}}$$

(3)where: Yf (System Yield) is the system daily useful energy, referred to the nominal power [kWh/kWp/day]; EACout is the amount of electrical energy generated by the PV power system; Pmax, STC is the total installed power of the PV array at standard test condition (STC).
The results of the financial efficiency analysis of grid-tied solar power systems with and without storage are carried out using Retscreen software. This software is used around the world to evaluate the energy production and associated savings, cycle costs, GHG emissions reductions, financial feasibility, and risks for renewable energy production or different energy efficiency technologies.
The financial feasibility indicators of the PV project are cash flow [31], payback period, and internal rate of return . The profitability, quality, and efficiency of a project are estimated from the internal rate of return (IRR), net present value (NPV), and benefit-cost ratio (B–C). The investment in a renewable power project has financial feasibility when the B–C is larger than 1, the IRR, and NPV are positive.

The internal rate of return IRR is the discount rate causing the Net Present Value (NPV) of the project to be zero.

$$0 = \sum_{n=0}^{N} \frac{C_n}{(1 + IRR)^n}$$

(4) where N is the project life in years, and Cn is the cash flow for year n.
The net present value NPV of a project is the value of all future cash flows, discounted at the discount rate, in today's currency.

$$NPV = \sum_{n=0}^{N} \frac{\widetilde{C}_n}{(1 + r)^n}$$

(5) where r is the discount rate, and $\widetilde{C}_n$
 is the after-tax cash flow in year n.
The benefit-cost ratio, B–C, presents the relative profitability of the project.

$$B - C = \frac{NPV + (1 - f_d)\,C}{(1 - f_d)\,C}$$

(6) where C is the total initial cost of the project, fd is the debt ratio.
The annual average reduction of CO2 uses the following formula:

$$tCO_{2e} = E\_Grid \times EFgrid$$

(7) where: E_Grid is the average annual generation of electricity from the solar power station (MWh), EFgrid is the CO2 emission factor of the Vietnamese power grid.

❖ CONVERSION OF SUNLIGHT INTO ELECTRICITY

Solar power can be converted directly into electrical power in photovoltaic (PV) cells, commonly called solar cells. The sun has a surface temperature of about 6,000°C, and its hot gasses at this temperature emit light that has a spectrum ranging from the ultraviolet, through the visible, into the infrared. According to quantum theory, light can behave either as waves or as particles, depending upon the specific interaction of light with matter; this phenomenon is called the wave-particle duality of light. In the particle description, light consists of discrete particle-like packets of energy called photons. Sunlight contains photons with energies that reflect the sun's surface temperature; in energy units of electron volts (eV), the solar photons range in energy (hv) from about 3.5 eV (ultraviolet region) to 0.5 eV (infrared region). The energy of the visible region ranges from 3.0 eV (violet) to 1.8 eV (red); the peak power of the sun occurs in the yellow region of the visible region, at about 2.5 eV. At high noon on a cloudless day, the surface of the Earth receives 1,000 watts of solar power per square meter (1 kW/m2). Photovoltaic cells generally consist of a light absorber that will only absorb solar photons above a certain minimum photon energy. This minimum threshold energy is called the "energy gap" or "band gap" (Eg); photons with energies below the band gap pass through the absorber, while photons with energies above the band gap are absorbed. The light absorber in PV cells can be either inorganic semiconductors, organic molecular structures, or a combination of both. In inorganic semiconductor materials, such as Si, electrons (e-) have energies that fall within certain energy ranges, called bands. The energy ranges, or bands, have energy gaps between them. The band containing electrons with the highest energies is called the valence band. The next band of possible

electron energies is called the conduction band; the lowest electron energy in the conduction band is separated from the highest energy in the valence band by the band gap. When all the electrons in the absorber are in their lowest energy state, they fill up the valence band, and the conduction band is empty of electrons. This is the usual situation in the dark. When photons are absorbed, they transfer their energy to electrons in the filled valence band and promote these electrons to higher energy states in the empty conduction band. There are no energy states between the valence and conduction bands, which is why this separation is called a band gap and why only photons with energies above the band gap can cause the transfer of electrons from the lower-energy-state valence band into the higher-energy-state conduction band. When photons transfer electrons across the band gap, they create negative charges in the conduction band and leave behind positive charges in the valence band; these positive charges are called holes (h+). Thus, absorbed photons in semiconductors create pairs of negative electrons and positive holes. In a PV cell, the electrons and holes formed upon absorption of light separate and move to opposite sides of the cell structure, where they are collected and pass through wires connected to the cell to produce a current and a voltage — thus generating electrical power. In organic molecular structures, the energy of the photons also must first exceed a certain threshold to be absorbed. This absorption creates an energetic state of the molecular system, called an excited state. These excited molecular states can also generate separated electrons and holes. Furthermore, certain organic polymers and other molecular structures can form organic semiconductors that provide the basis for organic PV devices. One difference between inorganic and organic PV cells is that in organic cells, the electrons and holes are initially bound to each other in pairs called excitons; these excitons must be broken apart in order to separate the electrons and holes to generate electricity. In inorganic PV cells, the electrons and holes created by the absorption of light are not bound together and are free to move independently in the semiconductor.

CdTe-based solar technology has achieved one of the lowest levelized costs of electricity among all energy sources as well as state-of-the-art field stability. Yet, there is still ample headroom to improve. For decades, mainstream technology has combined fast CdTe deposition with a $CdCl_2$ anneal and Cu doping. The resulting defect chemistry is strongly compensated and limits the useful hole density to ~10^{14} cm^{-3}, creating a ceiling for fill factor, photovoltage and efficiency. In addition, Cu easily changes energy states and diffuses spatially, creating a risk of instabilities that must be managed with care. Here, we demonstrate a significant shift by doping polycrystalline $CdSe_xTe_{1-x}$ and CdTe films with As while removing Cu entirely from the solar cell. The absorber majority-carrier density is increased by orders of magnitude to 10^{16}–10^{17} cm^{-3} without compromising the lifetime, and is coupled with a high photocurrent greater than 30 mA cm^{-2}. We demonstrate pathways for fast dopant incorporation in polycrystalline thin films, improved stability and 20.8% solar cell efficiency.

resulting in a bicontinuous network with low domain purity, which is detrimental to carrier transport. In addition, the application of solar cells in building structure intergradation requires more flexible form factor and large light-receiving angle tolerance to ensure a more constant power output upon daytime solar radiation angle change. Thus, manipulating the thin film morphology of APSCs from nano to micron length scales to enable strong light trapping, high carrier generation efficiency, and fast carrier transport is critical for efficiency improvement as well as light-receiving angle tolerance. In order to address the above-mentioned challenges, we devel- oped a consequential processing methodology to induce nano-to- micron sized hierarchical morphology based on the state-of-the-art PM6:PY-IT all-polymer blends10–12. The critical knack is to synergize the
effect from the phase-transitional solid additive of 1,4-diiodobenzene
(DIB)2,13, thermal annealing and solvent vapor annealing (SVA)14,15 post- treatments. A more effective control on the conjugated polymer crystallization is achieved through the controlled removal of solvent and solid additive, by which the polymer crystallization kinetics and thin film surface structure can be manipulated. A high crystallinity interconnected double-fibril network morphology is

obtained, show- ing superiority in generating high exciton splitting and high carrier transport[14]. And the DIB diffusion and removal onto thin film top surface leads to difference in modulus and tension, making mechanical
instability between the surface layer and the bulk[16–18]. Surface wrinkle
pattern is created, and the nano-sized fibril network is obtained and integrated within the bulk and surface. In the subsequent SVA treat- ment, the swelling and re-drying of the blended thin film cause shrinkage[19], leading to the change of wrinkle pattern from ridge to island. This morphology is an important milestone comparing to the previous nano-sized morphology optimization, in which such mor- phology can induce favorable optical trapping for photoactive thin films. The combinate nanoscale phase separation and micro surface pattern leads to an unprecedented high PCE of 19.06% (certified 18.59%) for APSCs. A large solar light receiving angle of unidirectional 50° is achieved (85% of the 0° PCE). These advances endow easier intergradation of OSC devices for commercial application scenarios. The power output at summer solstice in Shanghai city is calculated, which shows a ~30% improvement. The development of the surface-to- bulk hierarchical morphology can be as important as to the surface pattern for silicon solar cells. The high efficiency, high stability, and high-power output visualize the high potential commercial application for APSCs.

Results
The significance of surface pattern The surface pattern fabrication is a milestone for silicon solar cells[20,21], which serves as light trapping structure to suppress the optical loss and increase the optical path[22,23]. Dating back to 1986 at the University of New South Wales, surface optical structure has become the key technology for silicon cells that enables efficiency breakthrough over 20%[24]. And subsequently, silicon solar cells experienced vigorous developments. Developing surface structure for OSC can be more difficult due to the flow levering of solution processing methods. We have tried thin film buckling of P3HT:PC71BM blends to induce surface patterns by using the different mechanical strength of the OPV thin film and top electrodes[25,26] (relevant data is shown in Supplementary Fig. 1). However, this methodology is not compatible for the currently used high efficiency systems. Surface patterning methods such as photolithography and wet etching can be considered[27,28], which, however, induces much more complex device fabrication procedure. Thus, implementing surface pattern with a suitable morphology for OPV thin film is a challenging task. To obtain a rugged surface pattern to better utilize solar radiation, a unique surface formation mechanism needs to be developed. Here, surface pattern is achieved by using a phase transformative additive, which can crystallize and vaporize on a

semi-dried thin film. This idea is developed into a consequential pro- cessing method to induce hierarchical morphology, which not only optimizes the nano-sized fiber crystallites but also induces micron- sized surface optical morphology. Figure 1 shows the idea of optical structure in silicon solar cells and current efficient non-fullerene OSCs. The significant role of enhanced light absorption and light-receiving angle broadening originated from surface optical structure is expected to significantly improve the power output in daytime solar cell applications[22].

❖ Thin film fabrication and device performance
The optical properties of the flat and hierarchical thin films are com- pared. Figure 2a and Supplementary Fig. 2 show the chemical struc- tures and absorption features of PM6 and PY-IT. Chloroform (CF) is used as the fast-drying solvent while DIB is used as the phase trans- formative additive due to its easy sublimation nature. Carbon disulfide (CS2) solvent vapor annealing (SVA) is used to induce the thin film swelling. Thermal annealing (TA) is used to optimize morphology and synchronously vaporize DIB. These processing are combined in dif- ferent sequences to manipulate

the thin film morphology. The absorption of PY-IT in chloroform (CF) shows red-shift after adding DIB. As a result, a 12 nm red-shift can be seen when the DIB con- centration is 30 mg mL^{-1}, suggesting the planarization of molecular conformation of PY-IT under the presence of DIB. This feature could induce better ordering of PY-IT during film formation[29]. The TA and SVA treatments is used to refine the thin-film crystallization and bicontinuous network formation. The photoluminescence (PL) quenching experiment (Supplementary Fig. 3) was used to access the phase separation of blended thin films. It is seen that DIB and DIB/TA/ SVA processed thin films showed enhanced PL quenching efficiencies, which, in conjugation with enhanced crystallization, indicate a more efficient exciton diffusion for photoactive blends. A better-balanced mixing and phase separation condition is obtained in an optimized bicontinuous nano-sized morphology that supports the highly effi- cient exciton diffusion and dissociation.

We then investigate the morphology formation mechanism by comparing DIB with a conventionally used 1-chloronaphthalene (CN) additive. The thin film drying kinetics were shown in Supplementary Fig. 4. It is seen that CF solvent vaporizes within seconds which is not beneficial to the crystallization process of donor and acceptor mate- rials. On the other hand, CN additive dramatically prolongs the film drying, leaving longer time for molecular reorganization. However, DIB additive behaves differently. For the case of DIB, the solvent vaporizes quickly as that in CF processing to form a thin film. Then, a slow and steady DIB removal process is recorded, which is due to DIB diffusion and sublimation. The film thickness right after casting and post treatments were compared (shown in Supplementary Fig. 5). The DIB processed thin film showed an initial thickness around 200 nm. After TA treatment at 100 °C, the film thickness was quickly reduced to about 120 nm in seconds, which is close to natural film thickness processed without additive. The SVA treatment of DIB processed thin film further induced large sized DIB crystallization on surface, which could not be removed by TA. Thus, a controlled removal of DIB is critical. The detailed fabrication DIB/TA/SVA process is shown in Supplementary Fig. 6, and more details are summarized in Device Fabrication section.

The J-V curves and solar cell performances for the PM6:PY-IT blends are summarized in Fig. 2b and Table 1. The device optimiza- tion process is shown in Supplementary Fig. 7 and Supplementary Table 1. Supplementary Fig. 8 shows the energy levels of PM6 and PY- IT. The lowest unoccupied molecular orbital (LUMO) and highest occupied molecular orbital (HOMO) energy levels were estimated by cyclic voltammetry (CV). The LUMO/HOMO levels are −3.67/−5.60 eV for PM6 and −3.88/−5.71 eV for PY-IT. Thus, a heterojunction with a high built-in potential is expected (LUMO$_{PY-IT}$-HOMO$_{PM6}$). The as-
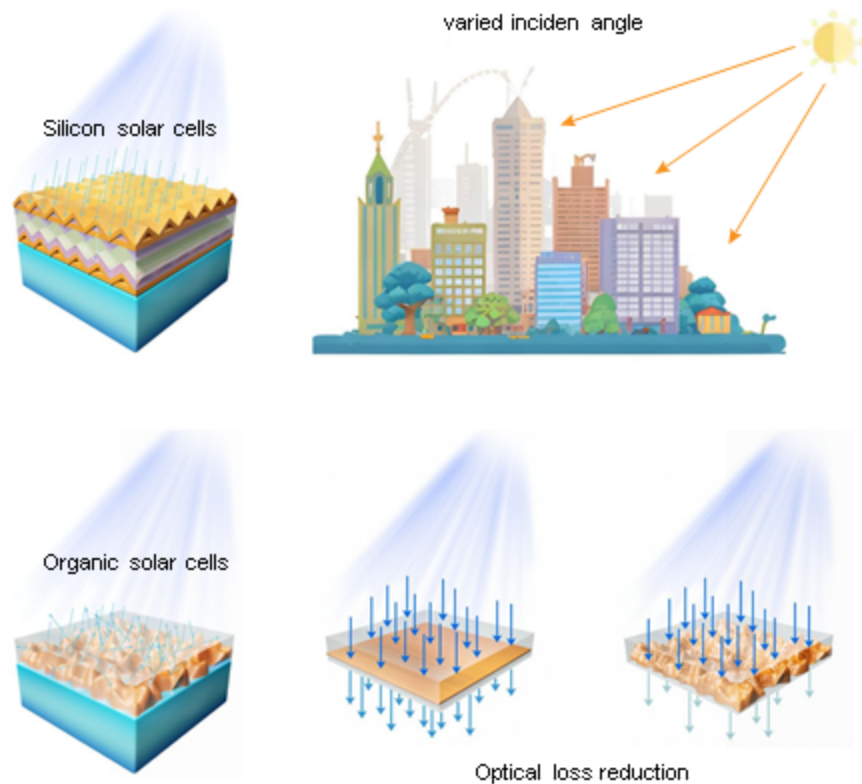
Fig. 1 | The past and present of surface topology and its significance on device function. The comparison of surface topography between silicon solar cells and organic solar cells is shown in the left two figures, and the lower right image shows

that the surface topography reduces light loss in organic solar cells. The figure on the top right indicates that organic solar cells with such surface topography are more suitable for urban environments.

cast, DIB and DIB/TA/SVA processed blends showed a PCE of 15.17% (VOC = 0.933 V,   JSC = 24.12 mA cm−2,   FF = 67.42%),   16.97% (VOC = 0.938 V,   JSC = 24.98 mA cm−2,   FF = 72.39%)   and   18.32% (VOC = 0.944 V,   JSC = 25.92 mA cm−2,   FF = 74.88%),   respectively. Moreover, unprecedented high efficiency of 19.06% is obtained with a VOC of 0.945 V, a JSC of 26.37 mA cm−2, and an FF of 76.48%, when the 2PACz was introduced as hole transport layer (HTL). Supplementary Fig. 9 shows the J-V curves. The optimum device obtained a third-party certified PCE of 18.59% (Supplementary Figs. 10−13), which is the highest value for APSCs. The higher VOC and JSC in DIB/TA/SVA processed thin film indicate that both carrier generation and carrier transport are optimized, suggesting that a more favorable mor-phology is obtained. Supplementary Fig. 14 shows the normalized performance of encapsulated device under continuous illumination over 1200 h under white light illumination of 1 sun intensity in air. The DIB/TA/SVA device efficiency stabilizes at around 800 h, which is ahead of DIB (around 950 h) and as-cast (1100 h) devices. The steady- state efficiency of DIB/TA/SVA device remained at 80% compared with 74% for DIB device and 68% for as-cast devices. These results imply that the morphology of DIB/TA/SVA device is more stable. The external quantum efficiencies (EQEs) and

differences are shown in Fig. 2c and Supplementary. It is seen that DIB/TA/SVA pro- cessing improved EQE value by ~4% with a wide wavelength range (from 350 nm to 840 nm), which originates from the improved exciton dissociation and carrier collection. As for DIB/SVA/TA con- dition, high concentration of DIB accumulates on the surface of the active layer, which reduces carrier extraction and results in lower EQE . The internal quantum efficiency (IQE) and EQE are further simulated electro-optically based on optical transfer matrix anddrift diffusion model. The optical constants of refractive- index (n) and extinction-coefficient (k) for the blends and all ancillary layers are shown in Supplementary. The comparison of simulated results and measured value are summarized in Supple- mentary. The solid line represents experimental results, while the dash line is simulation results. The simulation results are in well agreement with the test results, which validates the highest EQE/IQE value of DIB/TA/SVA processed device, and confirms the elevation of JSC. We further simulate the changes of EQE as a function of junction thickness. The shape of EQE profiles becomes flat when the film thickens increases. For the active film of 120 nm, most of the photons at absorption dip around 660 nm can be utilized, which contributes to improved Jsc and agrees well with the measured result. These results set the basis for thickness optimiza- tion, and explain the fundamental reason of the differences between absorption and EQE profiles. The statistical PCE for different device preparation conditions is summarized in Fig. 2d, which demonstrates the good reproducibility of the device performance and high relia- bility of the processing strategy. An explicit comparison to the state- of-the-art APSC performance is given in Fig. 2e and Supplementary based on the current results and 95 data points from 69 lit- eratures, from which we see that the newly develop APSC blends and morphology enable best balanced JSC and VOC.

Nano-to-micron morphology characterization
We investigated the nanoscale morphology of blended thin films. Grazing incidence wide-angle X-ray scattering (GIWAXS) was per- formed to study the polymer crystallization30. The scattering patterns and sector averaged curves in the in-plane (IP) and out-of-plane (OOP) directions are summarized in Fig. 3b and Supplementary.
Figure 3c underlined the difference of crystallization behavior under different processing methods. Comparing with the as-cast PM6:PY-IT blended film, crystallization improvements can be seen in the DIB and DIB/TA/SVA processed blends, since the ~0.28 Å−1 and the ~1.67 Å−1 peak intensity increases significantly. The crystalline coherence
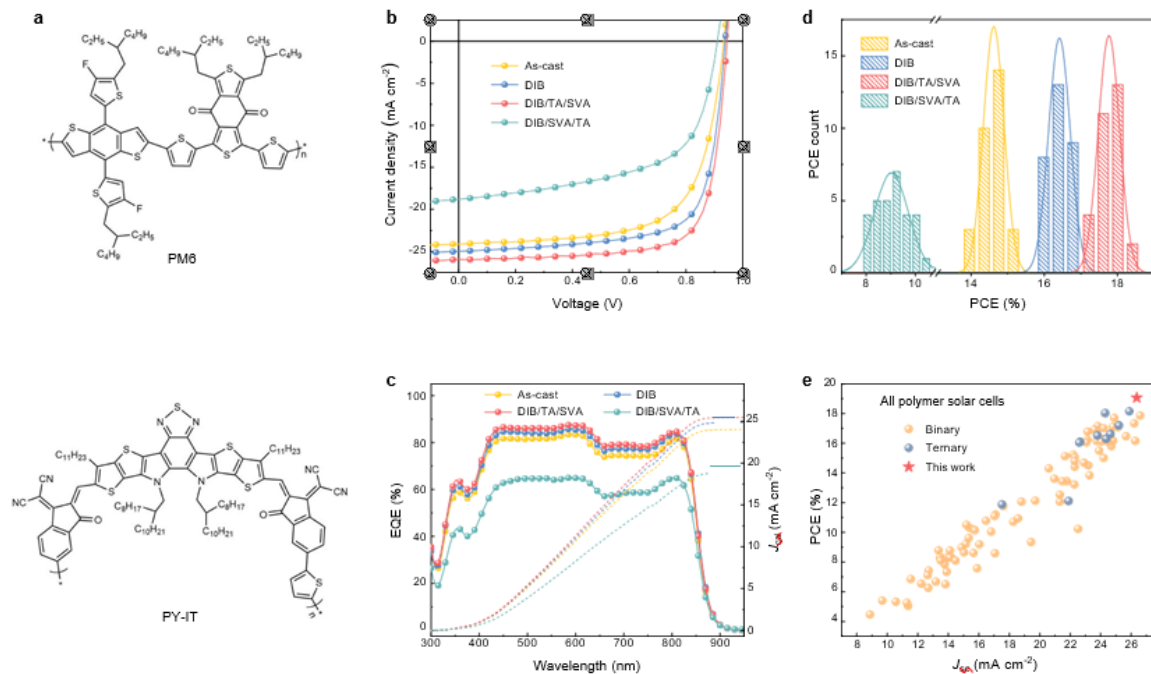
Fig. 2 | Materials and devices performances. a Chemical structures of PM6 and PY-IT. b J-V curves of the APSCs in different condition under AM 1.5 G, 100 mA cm−2. c EQE spectra of the APSCs in corresponding condition. All the DIB condition in text

is followed by a TA process. d Histogram of PCE measurement for devices of the APSCs in corresponding condition under AM 1.5 G, 100 mA cm−2. e Plots of the PCE versus JSC for the efficient all-PSCs reported in the literature.

Table 1 | Photovoltaic performance under simulated AM 1.5 G illumination

PM6:PY-IT	J_{SC} (mA cm^{-2})	J_{Cal} (mA cm^{-2})	V_{OC} (V)	FF (%)	PCE^a (%)
As-cast	24.12 (23.74 ± 0.18)	24.03 (23.79 ± 0.14)	0.933 (0.929 ± 0.003)	67.42 (66.26 ± 0.79)	15.17 (14.62 ± 0.28)
DIB	24.98 (24.41 ± 0.18)	24.87 (24.62 ± 0.13)	0.938 (0.937 ± 0.002)	72.39 (71.63 ± 0.85)	16.97 (16.42 ± 0.30)
DIB/TA/SVA	25.92 (25.38 ± 0.25)	25.48 (25.21 ± 0.14)	0.944 (0.941 ± 0.002)	74.88 (74.40 ± 0.49)	18.32 (17.76 ± 0.29)
DIB/SVA/TA	18.79 (18.08 ± 0.87)	18.82 (18.59 ± 0.17)	0.910 (0.905 ± 0.009)	59.64 (55.10 ± 2.86)	10.20 (9.03 ± 0.69)
DIB/TA/SVA^b	26.37 (25.96 ± 0.20)		0.945 (0.940 ± 0.003)	76.48 (76.10 ± 0.48)	19.06 (18.56 ± 0.18)
Certified	26.26		0.945	74.95	18.59

aThe average values are obtained from repeatedly individual experimental results.
bThe device prepared with 2PACz as HTL.

lengths (CCLs) fitted for the lamellar stacking peaks (Supplementary Tables 2–3) are 58, 70, 74 Å for as-cast, DIB, and DIB/TA/SVA processed blends, respectively. As for π-π stacking peaks, the CCLs are 17, 18, 19 Å for as-cast, DIB, and DIB/TA/SVA blends, respectively. Pronounced increase is seen for DIB/TA/SVA blends, indicating that the con- sequential processing enhances the ordering of π-π stacking. Such change mostly arises from TA/SVA treatment, which drives out DIB additive and induces fibrillar morphology formation. The improved π- π stacking is beneficial to charge transport and recombination prop- erties, thus better device performance is justified.

The phase separation of the blended thin films was investigated by atomic force microscopy (AFM) and transmission electron microscopy (TEM) (Supplementary Fig. 22). The as-cast film shows a homogeneous mixing morphology. A fibrillar-type morphology is seen for DIB and DIB/TA/SVA blends, suggesting that the enhanced crystallization assists the growth of polymer fibrils. Atomic force microscopy-based infrared spectroscopy (AFM-IR) was used to probe the fibril structure in the DIB/TA/SVA blends[31,32], using the specific infrared (IR)

absorption at 1650 and 2215 cm^{-1} for PM6 and PY-IT, respectively. As shown in Fig. 3a, PM6 and PY-IT show well- resolved interconnected fibrillar structures with an averaged width of ~15 nm. The inter-fibril distance is of ~30 nm, as estimated by the line- cut profiles. The carbon and nitrogen K-edge resonant soft X-ray scattering (CK-RSoXS and NK-RSoXS) were performed at 285.6 and 399.8 eV to study the phase separation statistics (Supplementary Fig. 24)[33,34]. At 285.6 eV, scattering contrast rising from C 1 s → π* transitions delocalized over the π-conjugated polymer backbones. For DIB and DIB/TA/SVA blends, scattering shoulders are seen at ~0.014 and ~0.017 Å^{-1}, corresponding to phase separation of 45 and 37 nm. At 399.8 eV, the scattering contrast stems from the N 1 s → π* transitions on PY-IT. The DIB and DIB/TA/SVA blends show weak shoulders at ~0.013 and ~0.017 Å^{-1}, corresponding to the PY-IT inter-fibril distances of 48 and 37 nm, respectively. Thus, a refined fibrillar morphology is obtained upon DIB/TA/SVA processing. This morphology is key in elevating the photophysical process of the photoactive layer to deliver higher JSC and FF.
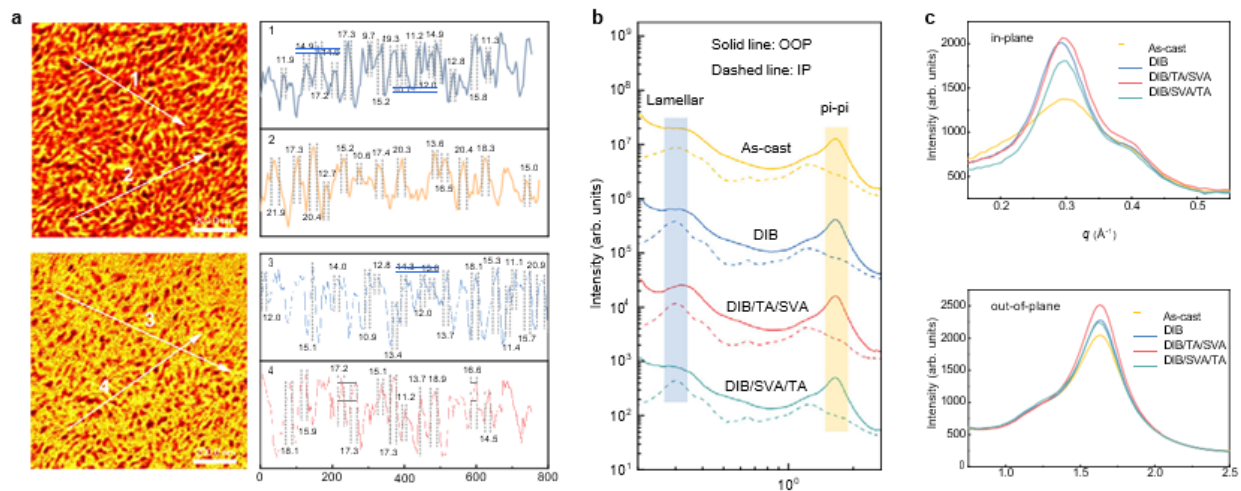

Fig. 3 | Nanoscale fibril crystallization morphology characteristics. a Tapping AFM-IR image at the wavenumber of 1650 cm^{-1} and 2215 cm^{-1} in optimal DIB/TA/SVA condition. b Line cut profiles for

PM6:PY-IT blends in different conditions. c Individual in plane and out of plane line cut profiles of the 2D GIWAXS data.

On top of the nano-sized bicontinuous morphology, a micron- sized topology is seen for sequentially processed thin films. Optical
microscope, surface profiler, and AFM were used to reveal the struc- ture details. As shown in Fig. 4a–c and Supplementary, DIB processed thin film displays a uniform surface over hundreds of micrometers. TA treatment leads to ridge structure in tens of microns. After subsequent SVA treatment, island microstructure is formed. The TA and SVA processing sequence cannot be changed since the con- trolled removal of DIB is key. SVA on DIB processed thin film results in large sized DIB spherical crystals and covers the entire film surface. The DIB/TA/SVA surface features are clearly visualized by surface profilometer and AFM. The island struc- ture affords diffusive reflection to trap light and improve device per-
formance from back as that in silicon solar cells in front35. We measured the angle dependent device performance of solar cells (Fig. 4d–f and Supplementary Table 4). For DIB/TA/SVA device, a 16.76% PCE is obtained at an incident angle of 50°. For comparison, the
flat device (as-cast) showed a 11.02% PCE at the same angle of inci- dence. In this scenario, higher daytime total energy production and more flexible installation geometry can be obtained. The developed sequential processing was extended to a few commonly used OSC blends (Fig. 4e, Supplementary, and Supplementary Tables 5–8), encouraging results were obtained. Thus DIB/TA/SVA processed can be a widely used strategy to induce nano-to-micron hierarchical morphology to enhance light receiving angle responses.

Device physics and photophysical processes
To reveal the function of surface pattern, we performed the optical electric field $|E(x)2|$ distribution simulation using transfer matrix method and measured n and k as shown in Supplementary to evaluate the impact of surface feature on light field distribution in photoactive thin film under varied light incident angles. Supplemen- tary show the results of flat device (as-cast), and Supple- mentary show the results of rugged device (DIB/TA/SVA). It is seen that even at the very small light incidence angle (for example 0° deviation angle in Supplementary the device with rugged
surface shows less optical loss due to light trapping effect. This trend is remained for all light incidence angles. Thus, the sequential DIB/TA/ SVA processed device shows less optical loss and larger JSC. The 2D volume integration of light fields is summaried in Supplementary Table 9. The detailed value is compared with measured JSC in Supple- mentary. The solid blue line and red line represent the JSC for as-

cast and DIB/TA/SVA condition at different incident angles, respec- tively. The dash blue line and red line represent the 2D integrate value of light field distribution for as-cast and DIB/TA/SVA condition at dif- ferent incident angles, respectively. The simulation results are in good agreement with the experimental value, revealing the advantage of the rugged surface feature of DIB/TA/SVA processed device. The impact of light incidence angle on power generation is estimated using the summer solstice of Shanghai city. The power gain is calculated using the solar radiation data at device operation conditions (Fig. 4g). The changes of zenith angle (θZ) during summer solstice is shown in Sup- plementary Table 10. The calculated the power output of the devices is shown in Fig. 4h, Supplementary, and Supplementary Table 11. It is seen that the power generation for DIB/TA/SVA processed device is increased by ~30%, which is a big leap for solar cells in application. It should also be noted that the improved light incidence angle response for DIB/TA/SVA processed device is beneficial for varied installation conditions (flat, tilted, or even vertical), which solves the form factor limitation in building integrated applications.

The synergy of nano fibril network and rugged surface pattern contributes to the improved photon-to-carrier conversion. The spec- tral and temporal characteristics of the charge-transfer dynamics in blended thin films are studied using the transient absorption spec- troscopy (TAS)36,37. The exciton diffusion lengths (LDs) for as-cast, DIB, DIB/TA/SVA processed neat PY-IT films are 35 nm, 38 nm, and 40 nm, respectively (Supplementary Table 12). Thus, PY-IT has an intrinsic high LDs that facilitates light extraction. An 800 nm excitation is used to excite PY-IT only, which is the major avenue of carrier generation. The 2D spectrum and representative TAS profiles at indicated delay times are shown in Supplementary. The decay traces at ~850 nm represent the ground-state bleach (GSB) of PY-IT, and the decay traces at around 910 nm are assigned to excited states absorption (ESA) of PY-IT. With the decay of the PY-IT bleach peak (850 nm), the PM6 GSB peak at around 595 nm rises, suggesting the hole-transfer process from PY-IT to PM6. These profiles are summarized in Fig. 5a, and fitted by biexponential function to obtain the kinetics (Supplementary Table 13). The fast components ($\tau 1$) represent the kinetics of the exciton dissociation in mixing domain or at interfaces, which are 0.53, 0.45 and 0.42 ps for the as-cast, DIB, and DIB/TA/SVA processed blends, respectively. The slow components ($\tau 2$) represent the kinetics of exciton diffusion in crystalline domain to interfaces, which are 13.71, 12.07 and 11.37 ps for the as-cast, DIB, and DIB/TA/SVA processed blends, respectively. The reduced $\tau 1$ indicates
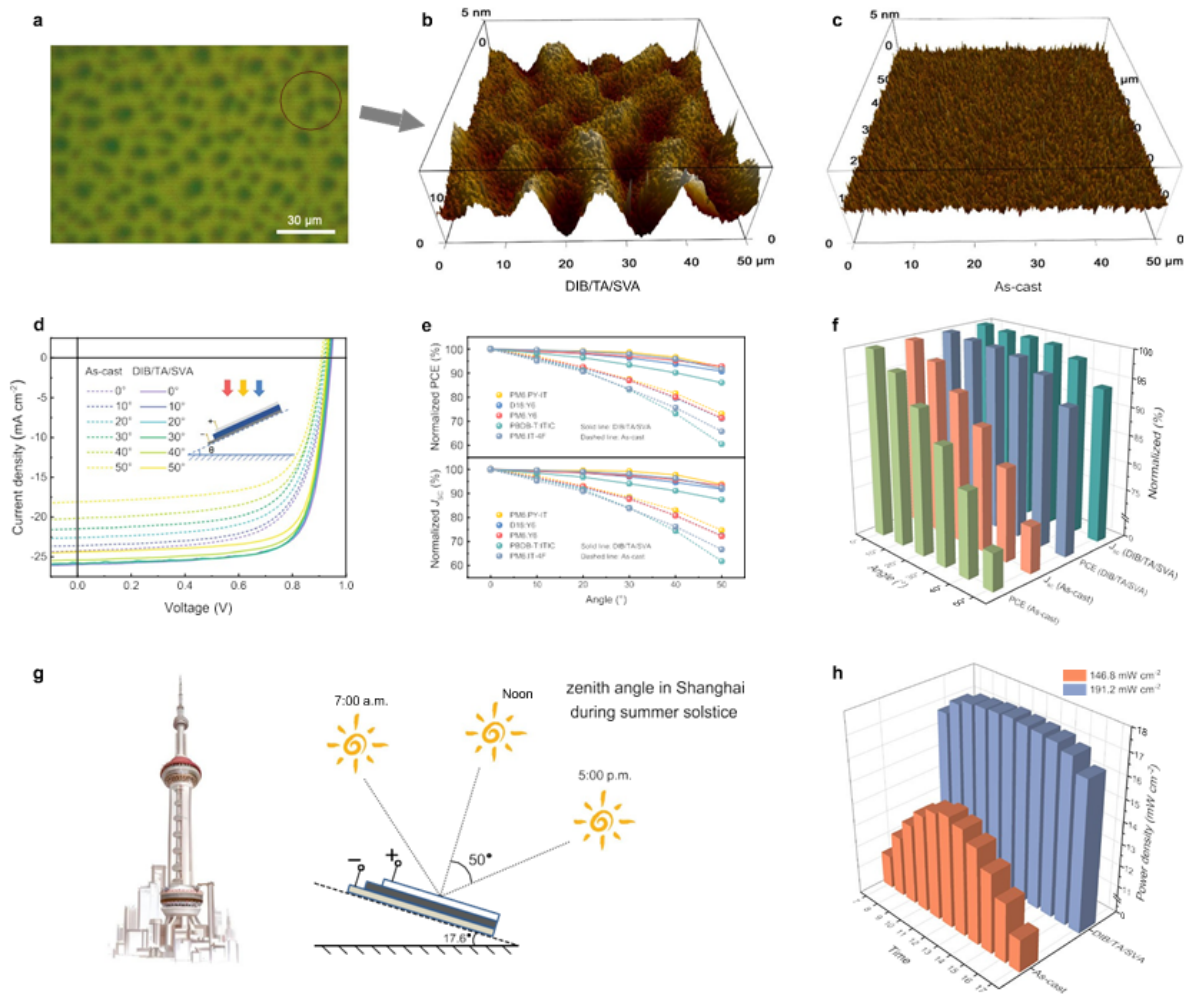
Fig. 4 | Microscale surface optical morphology characteristics. a Optical microscope photograph of DIB/TA/SVA. b Three-dimensional AFM photograph of DIB/TA/SVA. c Three-dimensional AFM photograph of as-cast. d J-V curve of as-cast and DIB/TA/SVA as function of light receiving angle. e Universality test for variable

angle experiment. f Variation of JSC and PCE of as-cast and DIB/TA/SVA device in different light receiving angle. g Scheme for daily power output simulation at the summer solstice in Shanghai. h Efficiency corresponding to the incident angle at different times in as-cast and DIB/TA/SVA condition.

that DIB/TA/SVA processing leads to a more favorable donor-acceptor interaction in mixing region, thus hole-transfer process is expedited. The decreased τ2 upon enhanced crystallization suggests an enhanced diffusion constant, which is associated with better crystalline packing in PY-IT fibrils. As shown in Fig. 5b, the DIB/TA/SVA blends show the optimal combination, which is characterized by longer exciton and carrier diffusion length, and faster exciton splitting process. The peak at 780 nm in TAS is identified to be the positive polaron signal[38], and its

recombination kinetics. under different VOC conditions are summarized in Supplementary Fig. 37. Both τc and n for DIB/TA/SVA devices show higher value than those in other devices over the applied VOC region, which is ascribed to a reduced charge recombination, suggesting less defects and energetic disorder in DIB/TA/SVA blends. The charge lifetime as a function of charge density is shown in Fig. 5c, which follows an approximately exponential law of

$$n^\lambda$$

decay lifetimes (τp) are 1499, 1955 and 2152 ps for the as-cast, DIB, DIB/
TA/SVA processed blends, respectively (Supplementary Table 13).

$$\tau c = \tau 0$$

0

ð1Þ

Thus, the carrier recombination is much lower in DIB/TA/SVA blends,

which agrees well with the photocurrent density-effective voltage (Jph- Veff) characterization results. The carrier col- lection efficiency P(E, T) values are 96.09%, 97.20%, and 97.85%, for the as-cast, DIB, and DIB/TA/SVA blends, respectively, contributing to high JSC for corresponding devices. The charge transport and recombination were investigated by transient photovoltage (TPV) and transient photocurrent (TPC) measurements[39]. The fitted charge lifetimes (τc) and charge density (n)

where τ0 and n0 are constants, and the exponential factor λ is in rela-

tion to the non-geminate recombination order R (R = λ + 1). When bimolecular recombination is the dominant loss mechanism in device, R is approaching to be 2. When trap-assisted recombination is dominant, R is expected to be higher than 2. The DIB/TA/SVA device shows a minimum R of 2.30 with the maximum lifetimes, which indicates minimized non-geminate recombination. Similar conclusions can be drawn from light intensity (Plight)-dependent JSC and VOC measurements.
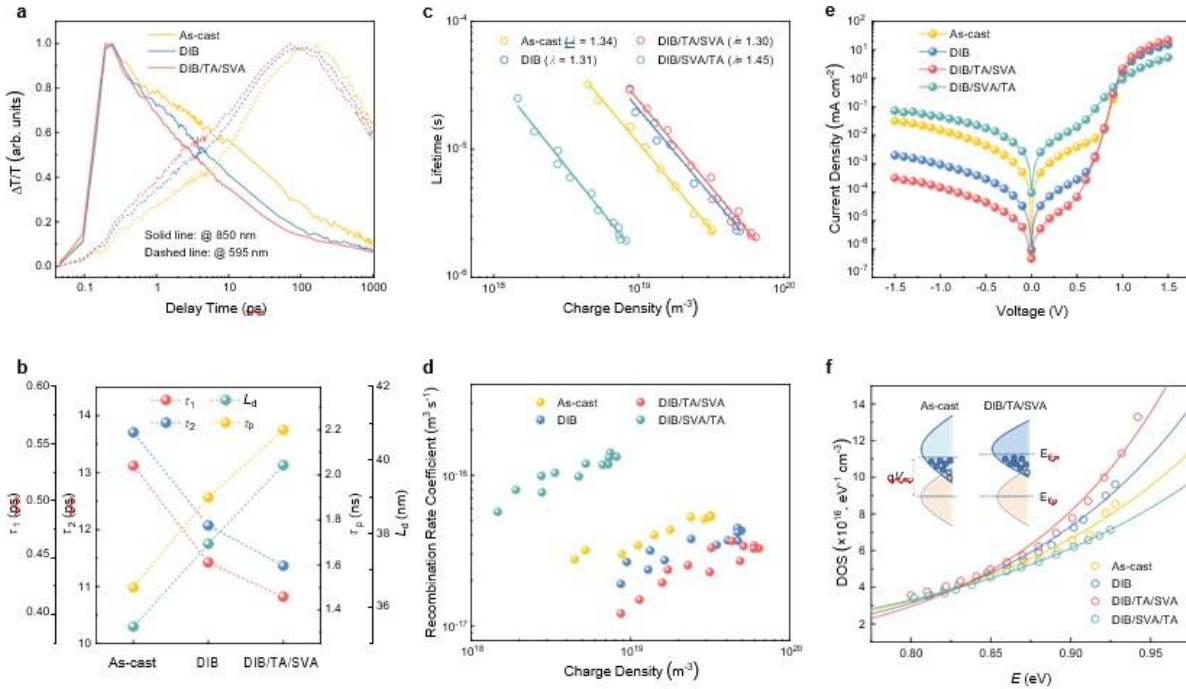
E (eV)

Fig. 5 | Ultrafast process and devices physical characteristics. a Hole transfer process kinetics in corresponding conditions. b Charge-transfer time and lifetime achieved through multi-exponential fitting in corresponding conditions. ($\tau 1$ is the fast components represent the kinetics of the exciton dissociation in mixing domain or at interfaces; $\tau 2$ is the slow components represent the kinetics of exciton diffusion in crystalline domain to interfaces; Ld is the exciton diffusion lengths; τp is

the fitted decay lifetimes for positive polaron signal). c Derived charge lifetime as a function of charge density fitted from TPV and TPC results (λ is the exponential factor). d Recombination rate coefficient as a function of charge density fitted from TPV and TPC results. e Dark J-V curves for corresponding conditions. f Derived LUMO DoS from the capacitance spectra of devices, inset is the schematic illustration.

The non-geminate recombination rate coefficient k(n) follows the equation of

and Fig. 5f, the as-cast device shows a Nt of 3.36×10^{18} cm^{-3} eV^{-1} and an Et of 139 meV. The DIB/TA/SVA device shows a much larger Nt of 1.28×10^{19} cm^{-3} eV^{-1} and a smaller Et of 99 meV, indicating a higher and

$$k_{d}n_{p} = \frac{1}{\tau_{c}\partial n\partial p \times n}$$

$$\delta 2P$$

narrower DoS distribution (inset in Fig. 5f). The device Nt agrees well with the n value obtained in TPC/TPV measurement, validating that the increased charge density is the major contribution to the JSC

where τc(n) is the carrier lifetime. The k(n) with different charge den- sities is shown in Fig. 5d40. A clearly suppressed recombination is seen for DIB/TA/SVA blended thin film over a wide range of charge den- sities. The space charge limits current (SCLC) measurement shown in Supplementary Table 15 and 9 also supports this result.

The dark J-V curves of devices are shown in Fig. 5e. The DIB/TA/ SVA device shows reduced reverse saturated current densities, indi- cating improved diode characteristics with a low leaking current. In the forward direction, the DIB/TA/SVA device shows an early transition from Ohmic to semiconductor zones and higher saturation value, indicating a higher charge density41,42. The calculated rectification ratios (frec) at ±1.0 V are 4.8×10^2, 7.6×10^3, and 7.1×10^4 for as-cast, DIB, and DIB/TA/SVA devices, respectively, which is in consistence with the FFs43. The fundamental electronic property of the blended thin films is studied by the electron density of state (DoS) characterization, fol- lowing the relationship of

$$g_n \eth E \flat = \frac{N_t}{E_t} \exp\left[\frac{E - E_{LUMO}}{E_t} \right] \qquad \eth 3\flat$$

where Nt is the total density per unit volume, ELUMO is the LUMO energy level, and Et is the energy for exponential tail distribution that describes energetic disorder44. As shown in Supplementary Table 16

improvement in DIB/TA/SVA devices. The enhanced DoS and reduced energetic disorder also help to reduce the non-radiative energy loss, as evidenced by the enhanced electroluminescence quantum yields . All characterization details are summarized in Supplementary **Methods.**

Discussion

The above-discussed results fully visualize the structure-property relationship of nano-to-micron hierarchical morphology on device performances. The intergradation of bicontinuous network on an island-like rugged surface topology yield unprecedented device per- formance and power output. To gain a panoramic view of the internal correlations of many factors, a multi-variable cross-correlation analysis is carried out using multiple parameters obtained from many inde- pendent observations. The correlation coef- ficients (r) represent the correlation strength. It is seen the area of lamellar and π-π stacking have a favorable r value with μe, μh, α and s, since the fibrillar morphology constructs efficient pathways for charge transport and suppresses recombination. The transport and recom- bination characteristics show a high r-value with JSC and FF. The main factor that determines JSC is the exciton dissociation process (τ1 and τ2), and high r-values between τ1/τ2 and JSC are recorded. The presence of surface pattern also plays a positive role in the increase of JSC. Likewise, surface pattern also contributes greatly on light-receiving

angle tolerance. The significantly improved FF in DIB/TA/SVA results from high mobility, high carrier density, and less recombination. The VOC also gets increased for hierarchical morphology devices due to better thin film electronic structure and device transport characters.

To conclude, a nano-to-micron hierarchical active layer mor- phology is achieved by using the phase transformative additive and sequential thin film processing strategies for all-polymer organic solar cells. As a result, the optimized nano-sized donor-acceptor fibrillar network integrated in micron-sized island-like rugged thin film surface can better trap the light radiation in the active layer, expedite the exciton-to-polaron conversion, and eventually lead to highly efficient light-to-electricity conversion and

large light-receiving incident angles. The synergy of the two unique features in morphology improve the photon and carrier extraction simultaneously, which yields an unpre- cedented efficiency of 19.06% with superior illumination stability up to 1200 h. In addition, elementary solar solstice power output estimation yields a ~30% increase for operation due to the benefit of large light- receiving angle, which also helps to reduce the limitation of installation form factors. These advances are highly beneficial for the commercial applications of organic solar cells.

Methods
Materials
All reagents and chemicals were purchased from commercial sources (Aldrich or Acros) without further purification. PM6 and PY-IT were purchased from Solarmer Materials Inc.

General methods
UV-vis absorption spectra were recorded in a 0.1 mm slit width cuvette on a Shimadzu spectrometer model UV-1800 with films on the quartz plates at room temperature. The morphologies of the nanostructures were characterized by transmission electron microscopy (TEM, JEM- 1400, JEOL, Japan). The GIWAXS characterization of the thin films was performed at the Advanced Light Source (ALS) on beamline 7.3.3 (Lawrence Berkeley National Laboratory, LBNL). The incidence angle was 0.16°, and the beam energy was 10 keV. Samples were prepared under device conditions on the Si substrates. RSoXS was performed at beamline 11.0.1.2 (ALS, LBNL). Samples were prepared under device conditions on the Si/PEDOT:PSS substrates, then placed in water and transferred to a silicon nitride window.

Device fabrication
All polymer solar cells with the structure of ITO/PEDOT:PSS/PM6:PY-IT/ PNDIT-F3N/Ag were fabricated. Patterned ITO glass was successively cleaned twice in an ultrasonic bath by detergent, deionized water, acetone and isopropyl alcohol for 15 min each and then dried under a dry oven. The precleaned substrates were treated in an ultraviolet- ozone chamber for 20 min, then a ~15 nm thick PEDOT:PSS (Clevious PVP AI 4083 H. C. Stark, Germany) thin film was deposited onto the ITO surface by spin-coating (4000 rpm) and baked at 150 °C for 20 min. The PEDOT:PSS solution was diluted by water in volume fraction 1:1. Active layer was fabricated by spin-coating mixed solution of PM6 and PY-IT (weight ratio of 1:1.2) in precursor CF solution (with 30 mg mL−1 solid additive of DIB) at the donor concentration of 7 mg mL−1, at 3500 rpm for 40 s on the PEDOT:PSS substrate in a nitrogen glove box, and then baked for 10 min at 100 °C. Then SVA treatment is done in an opaque jar, and ~200 microliter of carbon disulfide (CS2) is added to serve as swelling vapor in closed environment after ~5 min of SVA treatment, the blended thin film is taken out, and then it is washed by isopropanol (spin-coating at 3500 rpm for 30 s). The active layer (around 120 nm) was pre-coated by methyl alcohol at 3500 rpm for 30 s, and PNDIT-F3N (0.7 mg mL−1 in methyl alcohol with 0.3% acetic acid, v/v) was fabricated at 2600 rpm for 30 s on BHJ film. Finally, 120 nm thick silver layer was thermally evaporated at a base pressure of 1 × 10−6 mbar in an evaporate chamber. The evaporation thickness

was controlled by SQC-310C deposition controller (INFICON, Ger- many). The monomolecular layer of 2PACz as HTL is prepared was fabricated by spin-coating 0.3 mg mL−1 methanol solution at 3000 rpm for 30 s on the ITO substrate in a nitrogen glove box and baked for 6 min at 100 °C, then flushed by methanol at 4000 rpm for 20 s.

Device characterization
The J–V curves were measured with Keithley 2400 Source under the illumination of AM 1.5 G irradiation (100 mW cm−2) using a 150 W solar simulator (DM-40S3, SAN-EI ELECTRIC, Japan) in

glove box at room temperature. The J–V characteristics were measured along the forward scan direction from −0.2 to 1 V, with a scan step of 50 mV and a dwell time is 10 ms using a Keithley 2400 Source Measure Unit. EQE spectra were measured by using a solar-cell spectral-response measurement system (QE-R3011, Enlitech).

Reporting summary

Further information on research design is available in the Nature Portfolio Reporting Summary linked to this article.

Data availability

The data that support the plots within this paper and other findings of this study are available from the corresponding authors upon request. The raw data has been uploaded to the database. Source data are provided with this paper in the Materials Cloud database (https://doi.org/10.24435/materialscloud:g4-jw). Source data are provided with this paper.

References

1.   Zhang, M. et al. Single-layered organic photovoltaics with double cascading charge transport pathways: 18% efficiencies. Nat. Com- mun. 12, 309 (2021).

2.   Zhu, L. et al. Single-junction organic solar cells with over 19% effi- ciency enabled by a refined double-fibril network morphology. Nat. Mater. 21, 656–663 (2022).